Anisotropic Third-Harmonic Generation in Layered Germanium Selenide

Arindam Dasgupta, Jie Gao, and Xiaodong Yang**

Germanium selenide (GeSe) is a 2D layered material with an anisotropic crystal structure analogous to black phosphorus (BP). But unlike BP, GeSe is stable under ambient conditions and therefore provides more flexibility in building practical nanoscale devices. The in-plane anisotropic vibrational, electrical, and optical properties of layered GeSe originating from the low symmetry of its crystal structure are being explored mostly for building polarization-sensitive optoelectronic devices. However, the nonlinear optical properties of layered GeSe have not been investigated yet. Here, the anisotropic polarization-dependent third-harmonic generation (THG) from exfoliated thin GeSe flakes due to the low in-plane lattice symmetry is reported. Furthermore, it is also shown that the intensity and polarization state of TH emission can be controlled by the polarization state of pump beam. Moreover, it is demonstrated that the crystal's symmetry axes can be rapidly determined by characterizing the intensity profile of TH emission upon the excitation from radially or azimuthally polarized vector beam. The results of this study pave the way for realizing anisotropic nonlinear optical devices such as multiplexers, signal processors, and other prototypes for future on-chip photonic circuits and optical information processing.

1. Introduction

Nonlinear optical materials are essential for light generation and modulation in building various optical devices, such as ultrafast pulsed lasers,[1] pulse autocorrelators, frequency converters,[2] optical switches,[3] modulators,[4,5] photodetectors,[6] wavelength-division multiplexers, and optical memory.[7] However, conventional nonlinear optical devices mainly use bulk crystals like beta barium borate and lithium niobate suffering from low conversion efficiency and technical limitation for being integrated into modern nanoscale photonic devices. Recent emergence of 2D layered materials (2DLMs) with high nonlinear conversion efficiency and atomic scale thickness has provided an immediate solution to open up the possibility of realizing many nanoscale photonic devices, such as all-optical signal processors, data security chips, mode-locked/Q-switched lasers,[8] and ultrafast photonic circuits.[9–13] Therefore, in the past decade, a series of 2DLMs have been explored in this context. Several reports demonstrated strong second-harmonic generation (SHG) from transition metal dichalcogenides (TMD)[14–19] and hexagonal boron nitride (h-BN),[16] whereas third-harmonic generation (THG) has been observed in TMD[20,21] and graphene.[22–24] Additionally, SHG and THG are highly dependent on the crystal symmetry of 2DLMs[21,25–27] so that they can be utilized for optical probing of the crystal orientation and thickness.[14–16] Optical anisotropy in crystal structures is envisioned as a new degree of freedom for manipulation and modulation of light.[11–28] Hence, a new class of 2DLMs with high in-plane anisotropy including BP and ReS_2 has attracted tremendous attention, where the centrosymmetric crystals of these materials only support THG.[29–32] Although several reports demonstrated THG in BP, the fact that it is unstable in ambient conditions remains the main hindrance towards its practical device application. In that context, as a new 2DLM constituted to the group-IV monochalcogenide, germanium selenide (GeSe) has recently come into focus. GeSe has a crystal structure analogous to BP but is stable under ambient conditions. The in-plane anisotropy of GeSe has been exploited for demonstrating various optoelectronic and photovoltaic applications in solar cells,[33–35] polarization-sensitive photodetectors, and phototransistors.[36–39] Also, the anisotropy-related birefringence of GeSe has been explored for the potential of designing optical elements such as polarizers and waveguides.[40,41] However, there has not been any investigation on the nonlinear optical properties of layered GeSe yet.

Here, we demonstrate the anisotropic THG from exfoliated thin GeSe flakes and characterize the polarization state of third-harmonic (TH) emission. The TH response is found to be highly anisotropic depending on the incident linear polarization of pump beam. By correlating the polarized THG with the theoretically derived equations, we show that the anisotropy arises from the low-symmetry crystal structure of GeSe. We also explore how the polarization orientation of TH emission varies depending on the linear polarization of pump beam. Furthermore, we investigate the evolution of the intensity and polarization ellipticity of TH signal depending on the polarization state of pump beam.

Dr. A. Dasgupta, Prof. J. Gao, Prof. X. Yang
Department of Mechanical and Aerospace Engineering
Missouri University of Science and Technology
Rolla, MO 65409, USA
E-mail: gaojie@mst.edu; yangxia@mst.edu

The ORCID identification number(s) for the author(s) of this article can be found under https://doi.org/10.1002/lpor.201900416

DOI: 10.1002/lpor.201900416

Moreover, we show that the lattice orientation of GeSe flake can be promptly determined by measuring the intensity profile of TH emission from the flake upon the excitation from radially or azimuthally polarized vector beam. Our results not only provide a better understanding of the nonlinear light–matter interactions in in-plane anisotropic 2DLMs, but also can be harnessed to realize nanoscale anisotropic optical devices for frequency- and polarization-based multiplexing, demultiplexing, and encoding prototypes in optical information processing and communication.

2. Results and Discussion

2.1. Determination of Crystal Axes of GeSe Flakes

GeSe is a layered group-IV monochalcogenide with an orthorhombic crystal structure belonging to the *pnma* 62 space group,[39] as illustrated in **Figure 1**a. The puckered honeycomb lattice of GeSe resembles that of BP with lattice periods a = 10.840 Å, b = 3.834 Å, and c = 4.390 Å where the two principal crystallographic axes b (y-axis) and c (x-axis) represent the in-plane zigzag and armchair directions, respectively. Thereby, the crystal possesses strong in-plane anisotropy. The adjacent layers are stacked by weak van der Waals forces along the z-axis facilitating mechanical exfoliation of 2D thin GeSe flakes from the bulk crystal. Figure 1b,c show the reflection microscope image and scanning electron microscope (SEM) image of a typical exfoliated GeSe flake on a quartz substrate, respectively. The atomic force microscopy (AFM) image in Figure 1d confirms an atomically flat surface of the exfoliated GeSe flake. The thickness of this flake evaluated from the height profile in the inset of the AFM image is about 90 nm. High-resolution transmission electron microscope (HRTEM) image of an exfoliated flake in Figure 1e shows a lattice spacing of 2.9 Å and an intersection angle of 91°, which is consistent with the [011] set of planes of the orthorhombic GeSe crystal structure.[41] The selected area electron diffraction (SAED) pattern in Figure 1f further confirms the single-crystal nature of the exfoliated GeSe flakes where the spot patterns are identical with the surface normal to the [100] crystal zone axis.

Previous studies have demonstrated that the evolution of the intensity of parallel polarization component for A_g and B_g Raman modes as a function of the linear polarization angle of incident light can be used to identify the crystal directions (armchair and zigzag).[40–42] Here, angle-resolved polarized Raman spectroscopy is carried out on the GeSe flake shown in Figure 1a to determine its crystal directions. In Figure 1g, we plot the parallel polarization component of the Raman spectra evolving with the linear polarization angle of incident light, as the x-axis (0°) indicated in the inset of Figure 1b. A 632.8 nm He-Ne laser is used as the excitation source. Four Raman peaks are observed at 81, 149, 172, and 187 cm^{-1} that are assigned as A_g^1, B_{3g}, A_g^2, and A_g^3 modes, respectively. It is shown that the intensities of all the Raman peaks vary periodically, depending on the linear polarization angle of incident light. However, no obvious shifts in the Raman peak positions are observed. Considering R to be the Raman tensor for the Raman modes of GeSe, the Raman intensity (I) can be expressed as $I \propto |e_i \cdot R \cdot e_s|^2$ with e_i and e_s being the unit polarization vectors of the incident and scattered light. Therefore, the angle-dependent Raman intensities of A_g and B_g modes in the parallel polarization configuration for the orthorhombic GeSe crystal can be written as[41]

$$I\left(A_g\right) \propto \left(|b|\sin^2\theta + |c|\cos\phi_{cb}\cos^2\theta\right)^2 + |c|^2\sin^2\phi_{cb}\cos^4\theta \quad (1)$$

$$I\left(B_{3g}\right) \propto f^2\sin^2 2\theta \quad (2)$$

where b, c, and f are constants of the Raman tensor, θ is the linear polarization angle with respect to the crystal axis, and ϕ_{cb} represents the phase difference between b and c. The polar plots of the Raman intensities of A_g^1, B_{3g}, A_g^2, and A_g^3 modes as a function of the incident polarization angle θ in the parallel polarization configuration are shown in Figure 1h–k. All the experimental data points (black points) match well with the fitted curves (red curves) based on Equations (1) and (2). It should be noted that the A_g^1 Raman peak shows a periodic variation of 180° with the maxima along 90° and 270°, while the A_g^2 mode has a 90° periodic variation with a maximum at 90° and a local secondary maximum at 0°. In contrast, the four-lobe pattern of the A_g^3mode exhibits a maximum at 0° and a secondary maximum at 90°, while the B_{3g} mode shows a four-fold aniostropy with a period of 90° having the minimum intesities along 0° and 90°. Previous studies on anistropic crystals indicates that the Raman intensities of parallel polarization components of the A_g modes reach a maximum or secondary maximum value when the linear polarization angle is oriented along any of the crystal axes.[36,40–42] Therefore, 0° (x-axis) and 90° (y-axis) orientations can be identified as either armchair or zigzag direction of the GeSe crystal.

For further confirmation of the armchair and zigzag directions of the GeSe flake, we performed polarization-resolved absorption spectroscopy measurements. The in-plane anisotropy in the orthorhombic crystal structure of GeSe flake induces strong linear dichroism and hence a stronger optical absorbance is expected when the polarization angle of incident light is along the armchair direction of the GeSe flake.[41] Figure 1l plots the measured polarization-resolved absorption spectra in the wavelength region of 450–850 nm. The evolution of the absorbance (α) as a function of the polarization angle (θ) at two different wavelengths of 700 and 800 nm are plotted in Figure 1m,n, respectively. The measured data are fitted with a sinusoidal function of the form $\alpha(\theta) = \alpha_x\cos^2(\theta+\delta) + \alpha_y\sin^2(\theta+\delta)$ where α_x and α_y are the absorbance values when the incident light is linearly polarized along the x- and y-axes, respectively. Clearly, for both the cases, the measured absorbance reaches the maximum when the incident light is linearly polarized along the x-axis (0°). Therefore, the armchair and zigzag directions of the GeSe flake are identified as the x- and y-directions, respectively.

2.2. Anisotropic THG from Thin GeSe Flakes

Figure 2a is a transmission microscope image showing the TH emission from the area of the flake illuminated by a 1560 nm pump laser with the spot size of 2.5 µm. The spectrum of the TH emission in Figure 2b shows an expected peak at 520 nm, which is exactly one-third of the wavelength of pump beam. Figure 2c is a log-scale plot of the TH intensity as a function of the pump

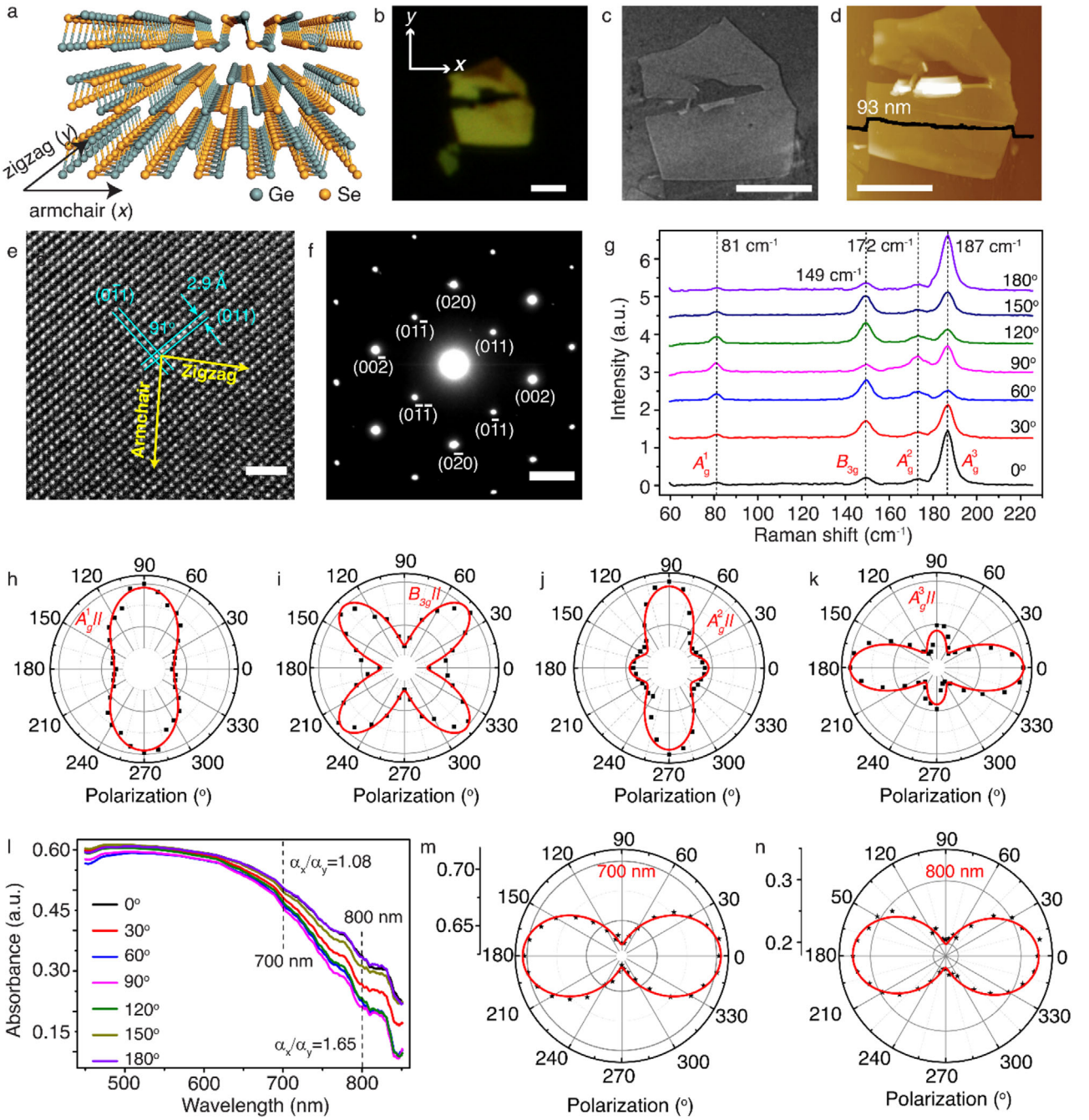

Figure 1. a) Schematic representation of the side view of the crystal structure of GeSe. b) Reflection microscope image of a typical exfoliated GeSe flake. *x*- and *y*-axes in the inset signify the reference axes. c) SEM image of the same flake. d) AFM image of the GeSe flake with the line profile in the inset shows that the flake is 93 nm thick and has an atomic smoothness. Scale bars are 5 μm. e) HRTEM image of the GeSe flake. Scale bar is 2 nm. f) Corresponding SAED pattern. Scale bar is 2 nm^{-1}. g) Raman spectra acquired in parallel polarization configuration from the GeSe flake for different polarization angles between 0° and 180° with respect to the *x*-axis. h–k) Polar plots of the Raman intensities of A_g^1 (81 cm^{-1}), B_{3g} (149 cm^{-1}), A_g^2 (172 cm^{-1}), and A_g^3 (187 cm^{-1}) Raman modes, respectively. Experimentally measured Raman intensities (data points) match well with the corresponding theoretical fits (red solid curves). l) Measured polarization-resolved absorption spectra for different linear polarization angles between 0° and 180°. m,n) Evolution of the measured absorbance (data points) as a function of the polarization angle at two different wavelengths of 700 and 800 nm. The red solid curves are the corresponding fits with the sinusoidal function.

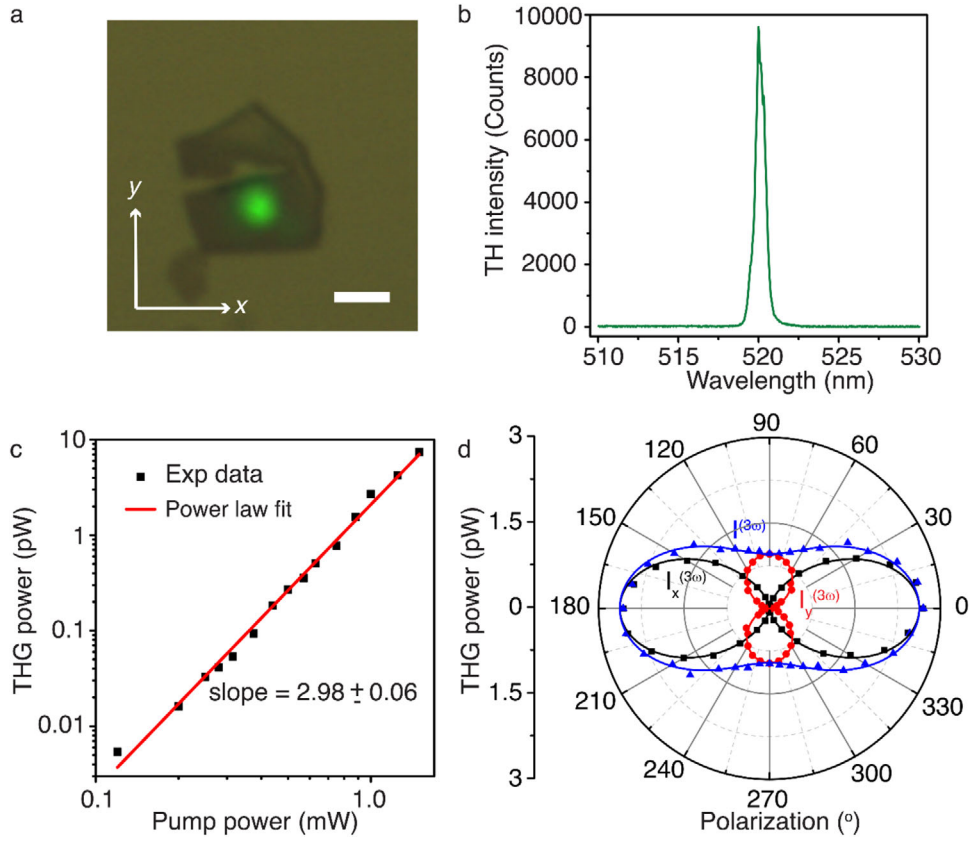

Figure 2. a) Transmission microscope image of the TH emission from the GeSe flake. Scale bar is 5 μm. b) Measured spectrum of THG emission with a peak wavelength at 520 nm, which is exactly one-third of the fundamental wavelength of pump beam at 1560 nm. c) Double log-scale plot of the measured average TH power as a function of the incident pump power. d) Angular dependence of the average TH power on the incident linear polarization. 0° corresponds to the *x*-axis (armchair direction of the crystal). Black, red, and the blue data points are experimentally measured *x*-component, *y*-component, and total TH intensity, respectively, while the solid curves are respective theoretical fits.

power, where the cubic power-law dependence further confirms the THG process. For an average pump power of 1.5 mW, we obtain a THG conversion efficiency of 4.9×10^{-9}.

Due to the highly anisotropic crystal structure, GeSe is shown to exhibit strong polarization anisotropy in the linear regime,[39,40] and a similar anisotropic nonlinear response is also expected. We consider the pump beam to be linearly polarized with the fundamental frequency ω, which can be expressed as, $\boldsymbol{E} = |\boldsymbol{E}|\hat{p}$ with $\hat{p} = \hat{x}\cos\theta + \hat{y}\sin\theta$ where θ is the polarization angle relative to the *x*-axis (armchair direction). Now, the contracted third-order nonlinear susceptibility tensor for the orthorhombic crystal of GeSe exhibiting THG can be written as follows[43,44]

$$\chi^{(3)} = \begin{bmatrix} \chi_{11} & 0 & 0 & 0 & 0 & \chi_{16} & 0 & \chi_{18} & 0 & 0 \\ 0 & \chi_{22} & 0 & \chi_{24} & 0 & 0 & 0 & 0 & \chi_{29} & 0 \\ 0 & 0 & \chi_{33} & 0 & \chi_{35} & 0 & \chi_{37} & 0 & 0 & 0 \end{bmatrix} \quad (3)$$

where the first subscript 1, 2, 3 refers to *x*, *y*, *z*, respectively, and the second subscript signifies the following

xxx	*yyy*	*zzz*	*yzz*	*yyz*	*xzz*	*xxz*	*xyy*	*xxy*	*xyz*
1	2	3	4	5	6	7	8	9	0

Therefore, the third-order nonlinear polarization component in GeSe crystal is

$$P^{(3\omega)} = \begin{bmatrix} P_x^{(3\omega)} \\ P_y^{(3\omega)} \\ P_z^{(3\omega)} \end{bmatrix} = \varepsilon_0 E \begin{bmatrix} \left(\chi_{11}\cos^3\theta + 3\chi_{18}\cos\theta\sin^2\theta\right) \\ \left(\chi_{22}\sin^3\theta + 3\chi_{29}\sin\theta\cos^2\theta\right) \\ 0 \end{bmatrix} \quad (4)$$

which yields the expression of the TH electric field to be $E^{(3\omega)} \propto P_x^{(3\omega)}\hat{x} + P_y^{(3\omega)}\hat{y}$. Thus, the *x*- and *y*-polarization components of the generated TH intensity can be expressed as

$$\begin{aligned} I_x^{(3\omega)} &\propto \left(\chi_{11}\cos^3\theta + 3\chi_{18}\cos\theta\sin^2\theta\right)^2 \\ I_y^{(3\omega)} &\propto \left(\chi_{22}\sin^3\theta + 3\chi_{29}\sin\theta\cos^2\theta\right)^2 \end{aligned} \quad (5)$$

From Equation (5), it is clear that the output TH emission is also linearly polarized where the polarization angle with respect to the *x*-axis is

$$\theta_{\mathrm{THG}} = \tan^{-1}\left(\frac{\chi_{22}\sin^3\theta + 3\chi_{29}\sin\theta\cos^2\theta}{\chi_{11}\cos^3\theta + 3\chi_{18}\cos\theta\sin^2\theta}\right) \quad (6)$$

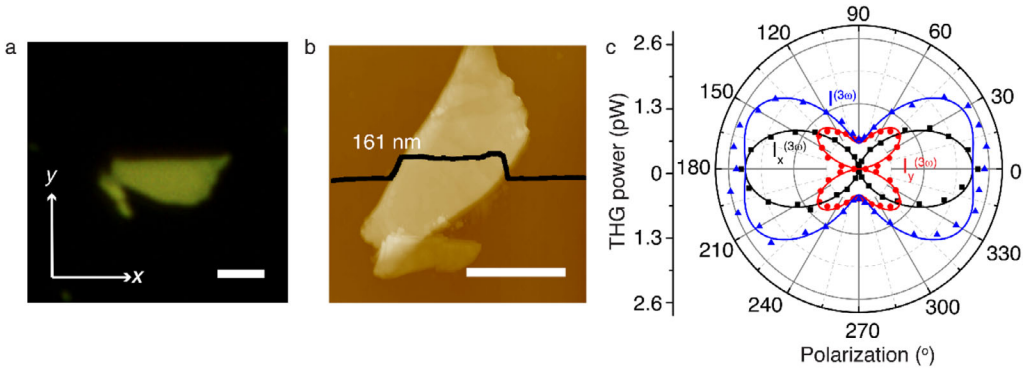

Figure 3. a) Reflection microscope image and b) AFM image of another GeSe flake with thickness of 161 nm. c) Corresponding angular dependence of *x*-component (black), *y*-component (red), and total (blue) average THG power on the incident linear polarization. Experimental measurements (data points) are fitted with respective theoretical fits (solid curves). All the scale bars are 5 μm.

First, the dependence of the TH intensity on the incident linear polarization of pump beam is characterized. The desired incident linear polarization of pump beam is obtained by placing a linear polarizer oriented along the armchair direction (*x*-axis, 0°) of the GeSe flake and a rotating half-wave plate (HWP). The blue triangles in Figure 2d show the angular dependence of the TH signal from the GeSe flake as a function of the incident linear polarization relative to the crystal armchair direction (*x*-axis), while the black and the red data points correspond to the measured *x*- and *y*-polarized components. It is evident that the maximum and the minimum in the TH response correspond to the incident linear polarization aligned along with the armchair and the zigzag direction (*y*-axis, 90°) of the crystal, respectively. The solid lines in Figure 2d are the fits to the measured data using the relationships in Equation (5), which shows that the measured data agrees very well with the theoretical model. The extracted relative magnitudes of the $\chi^{(3)}$ tensor components are $\chi_{11} : \chi_{18} : \chi_{22} : \chi_{29} = 1 : 0.249 : 0.603 : 0.224$. As expected, the $\chi^{(3)}$ tensor of the GeSe flake is highly anisotropic. It is noted that the shapes of the angle-dependent anisotropic TH intensity profiles from the exfoliated GeSe flakes can change slightly with the varying values of χ_{22} and χ_{29} components, which we observe for a different GeSe flake shown in **Figure 3**a. The AFM measurement on this sample shown in Figure 3b indicates that the thickness of this GeSe flake is around 160 nm. Figure 3c plots the polarization dependence of the measured TH signal as well as its *x*- and *y*-polarized components along with the corresponding theoretical fits. Unlike the previous case with a two-fold polarization-dependent pattern for $I_y^{(3\omega)}$, here a four-fold pattern for $I_y^{(3\omega)}$ is observed, where the maximum TH intensity does not occur when the incident linear polarization is along the armchair direction of the crystal. The obtained relative magnitudes of the $\chi^{(3)}$ tensor components in this case are $\chi_{11} : \chi_{18} : \chi_{22} : \chi_{29} = 1 : 0.262 : 0.478 : 0.495$. The fact that the value of χ_{29} is comparable to χ_{22} results in the four-fold polarization-dependent pattern for $I_y^{(3\omega)}$. The dissimilarities between the values of the $\chi^{(3)}$ tensor components in two scenarios may be attributed to the deformation in the crystal lattice during the exfoliation process. Such phenomenon has also been observed in the anisotropic THG in the exfoliated BP flakes.[29–32]

2.3. Thickness-Dependent THG in GeSe Flakes

Next, the dependence of the THG conversion efficiency on the thickness of GeSe flake is investigated. We choose seven exfoliated flakes with thicknesses ranging from 10 nm to 160 nm. Since the Raman peak position can indicate the thickness of the GeSe flake, first we explore the evolution of Raman spectrum as a function of the thickness of GeSe flake. **Figure 4**a plots the observed Raman frequency shifts in the A_g^1, B_{3g}, A_g^2, and A_g^3 modes by taking the peak position of each mode for the 93 nm-thick flake (Figure 1b) as the reference. By decreasing the flake thickness, all the A_g modes exhibit frequency redshift whereas the B_{3g} mode shows blueshift. Figure 4b plots the measured THG conversion efficiency as a function of the flake thickness. The average pump power is 1 mW, corresponding to a peak irradiance of 5.6 GW cm^{-2}. The conversion efficiency gradually increases to 2.7 ×10^{-9} as the thickness is increased from 10 to 60 nm and then remains almost the same.

To assess the THG conversion efficiency of GeSe flakes, we compare the current results with the already reported THG conversion efficiencies of graphene and other anisotropic 2DLMs such as BP and ReS_2. All the reported conversion efficiencies are charted in **Table 1**.

2.4. Polarization State Analysis of TH Emission

The polarization ellipticity ϵ_{THG} and polarization orientation θ_{THG} of the TH emission from the GeSe flake in Figure 1b is then measured as a function of the pump polarization orientation θ by determining the Stokes parameters of the TH signal as $S_0 = |E_x^{(3\omega)}|^2 + |E_y^{(3\omega)}|^2$, $S_1 = |E_x^{(3\omega)}|^2 - |E_y^{(3\omega)}|^2$, $S_2 = 2Re\{E_x^{(3\omega)} E_y^{(3\omega)}\}$, and $S_3 = -2Im\{E_x^{(3\omega)} E_y^{(3\omega)}\}$, with $\epsilon_{THG} = \tan(\frac{1}{2}\sin^{-1}\frac{S_3}{S_0})$ and $\theta_{THG} = \frac{1}{2}\tan^{-1}\frac{S_2}{S_1}$. **Figure 5**a plots the polarization ellipticity of the TH

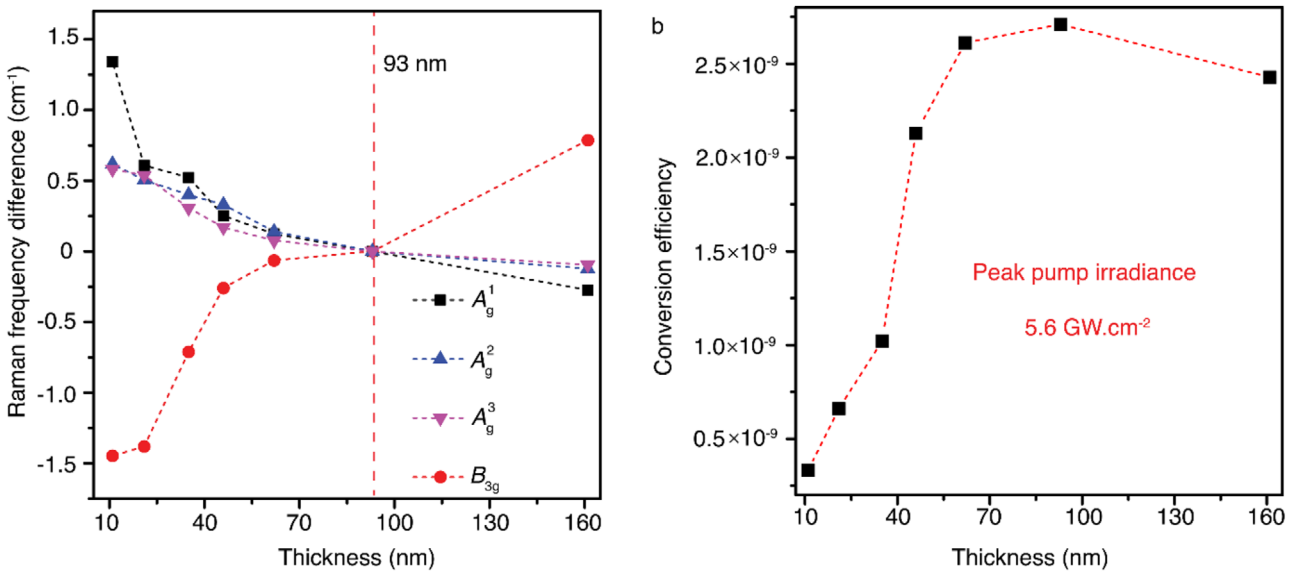

Figure 4. a) Thickness-dependent Raman frequency shifts, where the 93 nm-thick GeSe flake is used as the reference. b) THG conversion efficiency as a function of the thickness of GeSe flake under a pump irradiance of 5.6 GW cm^{-2}.

Table 1. Comparison of THG conversion efficiencies of various 2DLMs reported in literature.

Material	Thickness [nm]	Fundamental wavelength [nm]	Peak pump irradiance [GW cm^{-2}]	Conversion efficiency [$\times 10^{-9}$]	Reference
GeSe	10–100	1560	5.6	0.3–2.7	This work
BP	5–20	1557	≈8	≈0.01–0.1	[41]
BP	30	1560	≈440	≈2.8	[11]
ReS_2	Monolayer	1515	≈130	≈0.23	[32]
Graphene	Monolayer-multilayer	1560	≈186	≈0.02–3	[45]

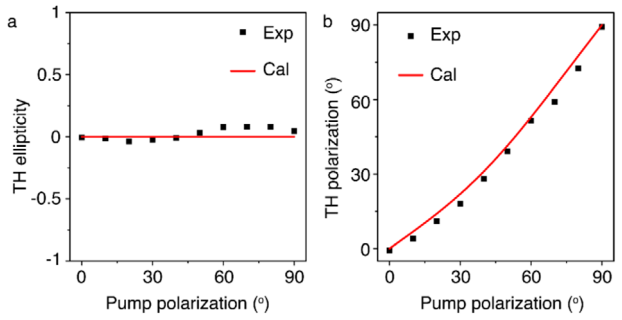

Figure 5. a) Evolution of the TH polarization ellipticity as a function of the pump polarization orientation. b) Evolution of the TH polarization orientation as a function of the pump polarization orientation.

emission as the incident linear polarization of pump beam is rotated gradually from 0° to 90°. Regardless of any incident linear polarization, the measured ellipticity remains almost zero indicating the output TH signal is indeed linearly polarized. Figure 5b plots the evolution of the polarization orientation of the TH emission as a function of that of pump beam. The experimentally determined polarization orientations (black data points) are consistent with the theoretical prediction (solid red curve) from Equation (6).

Next, the effect of in-plane anisotropy in the layered GeSe crystal on the intensity and polarization state of the TH emission is further explored upon the excitation from an elliptically polarized pump beam. The electric field of pump beam with the major axis of the polarization ellipse oriented along the armchair direction (x-axis) of the GeSe crystal is considered as $\boldsymbol{E} = |\boldsymbol{E}|\,\hat{e}_{\pm}$ where $\hat{e}_{\pm} = \hat{x}\,\cos\beta \pm \hat{y}i\sin\beta$ with β being the ellipticity angle. Hence, the electric field of the TH signal can be expressed as

$$E^{(3\omega)} \propto \left(\chi_{11}\cos^3\beta - 3\chi_{18}\cos\beta\sin^2\beta\right)\hat{x} + i\left(-\chi_{22}\sin^3\beta + 3\chi_{29}\sin\beta\cos^2\theta\right)\hat{y} \quad (7)$$

from which the expression of the TH intensity can be calculated as

$$I^{(3\omega)} \propto \left(\chi_{11}\cos^3\beta - 3\chi_{18}\cos\beta\sin^2\beta\right)^2 + \left(-\chi_{22}\sin^3\beta + 3\chi_{29}\sin\theta\cos^2\beta\right)^2 \quad (8)$$

Equation (8) shows that the generated TH emission is elliptically polarized where the polarization ellipse has the same

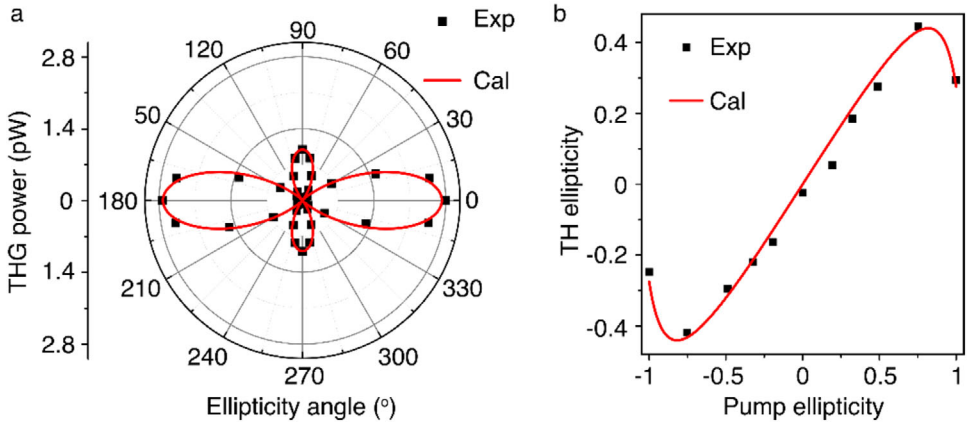

Figure 6. a) Dependence of the average THG power on the ellipticity angle of pump beam. 0° and 180° correspond to the linear polarization along the armchair direction; 90° and 270° correspond to the linear polarization along the zigzag direction; while 45°, 135°, 225°, and 315° correspond to the circular polarization. b) Evolution of the TH ellipticity as a function of the ellipticity of pump beam.

orientation as the pump beam. Also, the ellipticity of TH signal ϵ_{THG} is related to the ellipticity of pump beam ($\epsilon = \tan\beta$) by

$$\epsilon_{\mathrm{THG}} = \frac{-\chi_{22}\epsilon^3 + 3\chi_{29}\epsilon}{\chi_{11} - 3\chi_{18}\epsilon^2} \tag{9}$$

In the experiment, the desired elliptical polarization of pump beam is obtained by placing a rotating quarter-wave plate (QWP) before the sample while setting the initial incident polarization along the x-axis. Here, the ellipticity of pump beam is determined by the rotation angle of the QWP fast axis (β) with respect to the input linear polarization. Thus, depending on the ellipticity angle, the polarization state of pump beam varies from linear polarization $\beta = 0° + m \cdot 90°$ to circular polarization $\beta = 0° + m \cdot 45°$. The polar plot in **Figure 6**a shows the angular dependence of the TH intensity from the GeSe flake in Figure 1c as a function of β which follows the theoretical prediction of Equation (8). A four-lobe pattern with two unequal maxima is observed. The larger maxima for $\beta = 0° + m \cdot 180°$ is obtained as the pump beam remains linearly polarized along the armchair direction of the crystal, whereas the smaller maxima for $\beta = 90° + m \cdot 270°$ can be attributed to the fact that the incident pump polarization is rotated along the zigzag direction (y-axis) of the crystal. Also, the TH intensity becomes almost zero in the case of circularly polarized excitation. The ellipticity of TH emission ϵ_{THG} is then determined as a function of the ellipticity of pump beam ϵ by measuring the Stokes parameters. As shown in Figure 6b, when ϵ is gradually changed from from −1 (right-handed circular polarization) to +1 (left-handed circular polarization) by varying β from –45° to +45°, the measured TH ellipticity evolves according to the theoretical prediction of Equation (9).

2.5. Determination of Lattice Orientation with Vector Beam

Radially or azimuthally polarized vector beam is special as it carries all the linear polarization components equally distributed in its spatial intensity profile. Since the TH response of the GeSe flake is directly related to the high anisotropy of the crystal, the crystallographic information can be directly probed by imaging the TH intensity profile upon the excitation of the GeSe flake using the radially or azimuthally polarized vector beam. Due to the relatively larger doughnut-shaped spot sizes and the varying polarization components of the vector beams, we obtain a THG conversion efficiency of 1.3×10^{-10} with an incident pump power of 10 mW for both the vector beams. **Figure 7**a gives the TH image from the GeSe flake in Figure 1b (outlined by white dashed lines) when it is pumped with a doughnut-shaped radially polarized vector beam. It is evident that the TH signal has the minima along the y-direction as the spatial polarizations of pump beam at these positions are along the y-axis which corresponds to the zigzag direction of the lattice. While the maxima are observed in the x-direction as the polarizations of pump beam at these locations are oriented along the armchair direction. Figure 7b plots the TH intensity profile as a function of the azimuthal angle. The theoretically calculated plot is generated using Equation (4). Figure 7c shows the TH image in the case of the excitation with an azimuthally polarized vector beam. In contrast to the previous case, here the maxima and minima in the TH signal are observed along the y- and x-directions, respectively. The corresponding TH intensity profile depending on the azimuthal angle is shown in Figure 7d. Therefore, a very simple but efficient way for rapidly determining the crystal's principal axes of the GeSe flake is demonstrated, by imaging the anisotropic TH emission upon the excitation from radially or azimuthally polarized vector beam. It is noted that the polarization-dependent Raman,[40] photocurrent,[30] and THG[31] experiments are the existing methods for the crystallographic characterization of 2DLMs but require multiple measurements, whereas the current technique only needs to take one single TH image to provide the crystallographic information.

3. Conclusions

In conclusion, we have demonstrated the in-plane anisotropic THG from exfoliated thin GeSe flakes and performed polarization state characterization of the TH emission. First, the armchair and zigzag orientations of GeSe crystals are determined by

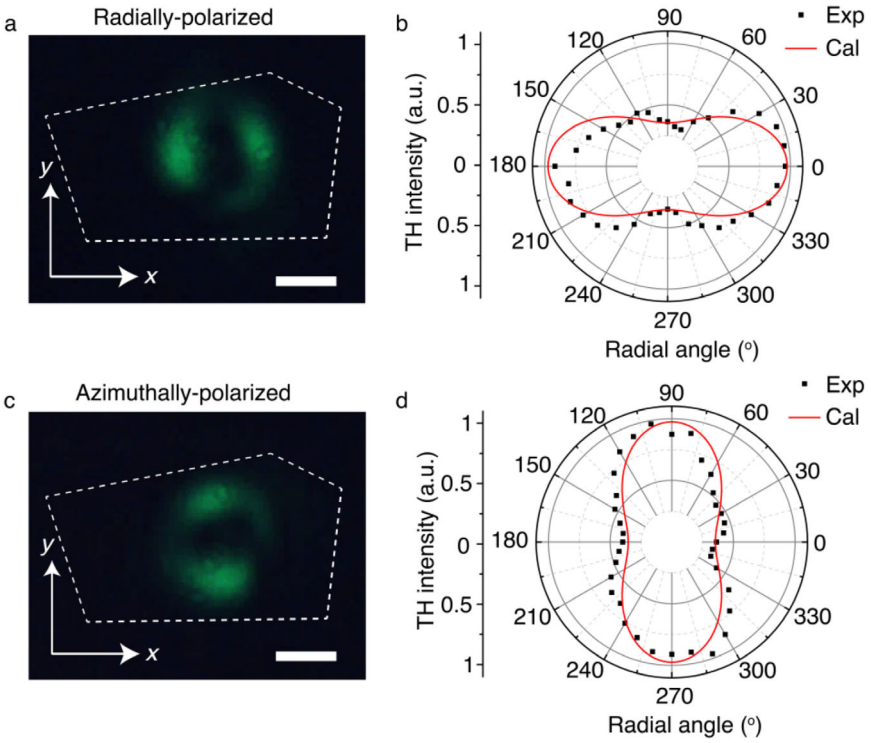

Figure 7. a) Measured TH image when the GeSe flake is excited with a radially polarized vector beam. *x*- and *y*-directions in the inset signify the armchair and zigzag directions of the crystal. The GeSe flake is outlined by white dashed lines. b) Corresponding TH intensity profile as a function of the azimuthal angle. Measured data (black data points) are fitted with theoretical profile (red solid curve). c) Measured TH image when the GeSe flake is excited with an azimuthally polarized vector beam. d) Corresponding TH intensity profile. Scale bars are 2 μm.

polarization-dependent Raman spectroscopy and linear absorption spectroscopy. By correlating the experimental data with theoretically derived equations, it is shown that the high anisotropy in THG depending on the incident linear polarization of pump beam is a result of the low in-plane lattice symmetry of GeSe. The relative magnitudes of the anisotropic $\chi^{(3)}$ tensor components of layered GeSe are also extracted. It is found that a small change in the $\chi^{(3)}$ tensor components will result in slightly different nature of the polarization anisotropy in the TH emission, which may be attributed to the deformation of the crystal during the exfoliation process. The dependence of the THG conversion efficiency on the GeSe crystal thickness is also explored. Furthermore, it is shown that the intensity and polarization state of TH signal can be precisely controlled by the polarization state of pump beam. In addition, it is demonstrated that the lattice orientation of GeSe flake can be promptly determined by characterizing the TH image from the flake upon the excitation from radially or azimuthally polarized vector beam. These results provide a fundamental understanding of anisotropic nonlinear light-matter interactions in 2D layered group-IV monochalcogenides. The demonstrated well-specified control over the intensity and polarization state of TH signal from layered GeSe can be harnessed for frequency- and polarization-based encoding, decoding and multiplexing of signals in optical communication and quantum information processing. The ultrathin nature of the group-IV monochalcogenide flakes also makes them ideal for building future on-chip anisotropic nonlinear optical devices.

4. Experimental Section

Sample Preparation: The quartz substrate was sonicated one after the other in deionized water, acetone, and isopropanol. The thin GeSe flakes were mechanically exfoliated from bulk GeSe crystals (2D semiconductors) using a scotch tape and then transferred onto the quartz substrate. For the TEM measurement, thin GeSe flakes were directly transferred onto a TEM grid by using a polydimethylsiloxane layer.

Optical Setup: A femtosecond laser pulse at the fundamental wavelength of 1560 nm (Calmar fiber laser, pulse width 90 fs, repetition rate 80 MHz) was transmitted through a linear polarizer and an HWP, and then focused onto the GeSe flake using a 20× objective lens (NA = 0.40). The transmitted TH emission from the GeSe flake was collected by a 50× objective lens (NA = 0.42), filtered spectrally to remove the transmitted fundamental pump beam, and then focused onto a color charge-coupled device (CCD) camera. For the spectral characterization of the TH intensity, a spectrometer (Horiba, iHR 520) was used instead of the color CCD camera. For the elliptically polarized excitation, after the HWP, a QWP was rotated in front of the GeSe flake. For the polarization ellipticity characterization of the TH emission, another combination of a QWP and a linear polarizer was inserted in front of the spectrometer. For the generation of radially and azimuthally polarized vector beam, the linearly polarized laser beam was passed through a zero-order vortex HWP (Thorlabs, WPV10L-1550) and then focused onto the GeSe flake.

For analyzing the Raman spectrum, a 632.8 nm He-Ne laser beam was passed through a linear polarizer and HWP and then focused on the GeSe flake using a 60× objective lens (NA = 0.85). The back-reflected light was collected by the same objective lens and directed towards the spectrometer using a beam splitter. The excitation laser was blocked by placing a Rayleigh rejection filter (Semrock, LP02-633RE-25) in front of the spectrometer. The parallel polarization component of the Raman spectrum was analyzed using another linear polarizer before the spectrometer.

For the polarization-resolved absorption measurement, light from a broadband white light source (Thorlabs, SLS201L, 360–2600 nm) was passed through a linear polarizer and focused on the GeSe flake using a 80× objective lens (NA = 0.5). The reflection spectrum was obtained by collecting the back-reflected light from the sample using the same objective lens and directing it towards the spectrometer with a beam splitter, while the transmission spectrum was collected using another 80× objective lens. After normalizing both the reflection and transmission spectra with the source spectrum, reflectance (R) and transmittance (T) were achieved. Finally the absorbance (α) spectrum was obtained by using the relation of $\alpha = 1 - (R + T)$.

Acknowledgements

The authors acknowledge support from the Office of Naval Research under grant number N00014-16-1-2408, and the National Science Foundation under grant numbers ECCS-1653032 and DMR-1552871. The authors also thank Wei-Ting Chen and Eric Bohannan for their help in acquiring the TEM and AFM images.

Conflict of Interest

The authors declare no conflict of interest.

Keywords

2D layered materials, germanium selenide, nonlinear optics, optical anisotropy, third-harmonic generation

Received: November 27, 2019
Revised: March 19, 2020
Published online:

[1] U. Keller, *Nature* **2003**, *424*, 831.
[2] M. H. Dunn, M. Ebrahimzadeh, *Science* **1999**, *286*, 1513.
[3] M. Scalora, J. P. Dowling, C. M. Bowden, M. J. Bloemer, *Phys. Rev. Lett.* **1994**, *73*, 1368.
[4] E. L. Wooten, K. M. Kissa, A. Yi-Yan, E. J. Murphy, D. A. Lafaw, P. F. Hallemeier, D. Maack, D. V. Attanasio, D. J. Fritz, G. J. McBrien, D. E. Bossi, *IEEE J. Sel. Top. Quantum Electron.* **2000**, *6*, 69.
[5] C. Wang, M. Zhang, B. Stern, M. Lipson, M. Lončar, *Opt. Express* **2018**, *26*, 1547.
[6] B. Nabet, *Photodetectors: Materials, Devices and Applications in Communications and Imaging Technologies*, Woodhead Publishing, Cambridge, UK **2015**.
[7] F. Bussières, N. Sangouard, M. Afzelius, H. de Riedmatten, C. Simon, W. Tittel, *J. Mod. Opt.* **2013**, *60*, 1519.
[8] B. Guo, Q. Xiao, S. H. Wang, H. Zhang, *Laser Photonics Rev.* **2019**, *13*, 1800327.
[9] A. Dasgupta, J. Gao, X. Yang, *Nano Lett.* **2019**, *19*, 6511.
[10] K. L. Seyler, J. R. Schaibley, P. Gong, P. Rivera, A. M. Jones, S. Wu, J. Yan, D. G. Mandrus, W. Yao, X. Xu, *Nat. Nanotechnol.* **2015**, *10*, 407.
[11] A. Autere, H. Jussila, Y. Dai, Y. Wang, H. Lipsanen, Z. Sun, *Adv. Mater.* **2018**, *30*, 1705963.
[12] N. Vermeulen, S. Palomba, *APL Photonics* **2019**, *4*, 060402.
[13] A. Dasgupta, J. Gao, X. Yang, *Sci. Rep.* **2019**, *9*, 8780.
[14] X. Yin, Z. Ye, D. A. Chenet, Y. Ye, K. O'Brien, J. C. Hone, X. Zhang, *Science* **2014**, *344*, 488.
[15] L. M. Malard, T. V. Alencar, A. P. M. Barboza, K. F. Mak, A. M. de Paula, *Phys. Rev. B* **2013**, *87*, 201401.
[16] Y. Li, Y. Rao, K. F. Mak, Y. You, S. Wang, C. R. Dean, T. F. Heinz, *Nano Lett.* **2013**, *13*, 3329.
[17] G. Wang, X. Marie, I. Gerber, T. Amand, D. Lagarde, L. Bouet, M. Vidal, A. Balocchi, B. Urbaszek, *Phys. Rev. Lett.* **2015**, *114*, 097403.
[18] C. Janisch, Y. Wang, D. Ma, N. Mehta, A. L.Elías, N. Perea-López, M. Terrones, V. Crespi, Z. Liu, *Sci. Rep.* **2015**, *4*, 5530.
[19] A. Autere, H. Jussila, A. Marini, J. R. M. Saavedra, Y. Dai, A. Säynätjoki, L. Karvonen, H. Yang, B. Amirsolaimani, R. A. Norwood, N. Peyghambarian, H. Lipsanen, K. Kieu, F. J. G. de Abajo, Z. Sun, *Phys. Rev. B* **2018**, *98*, 115426.
[20] R. I. Woodward, R. T. Murray, C. F. Phelan, R. E. P. D. Oliveira, T. H. Runcorn, E. J. R. Kelleher, S. Li, E. C. D. Oliveira, G. J. M. Fechine, G. Eda, C. J. S. D. Matos, *2D Mater.* **2016**, *4*, 011006.
[21] A. Säynätjoki, L. Karvonen, H. Rostami, A. Autere, S. Mehravar, A. Lombardo, R. A. Norwood, T. Hasan, N. Peyghambarian, H. Lipsanen, K. Kieu, A. C. Ferrari, M. Polini, Z. Sun, *Nat. Commun.* **2017**, *8*, 893.
[22] S. Y. Hong, J. I. Dadap, N. Petrone, P. C. Yeh, J. Hone, R. M. Osgood, *Phys. Rev. X* **2013**, *3*, 021014.
[23] N. Kumar, J. Kumar, C. Gerstenkorn, R. Wang, H. Chiu, A. L. Smirl, H. Zhao, *Phys. Rev. B* **2013**, *87*, 121406.
[24] R. Wang, H. C. Chien, J. Kumar, N. Kumar, H. Y. Chiu, H. Zhao, *ACS Appl. Mater. Interfaces* **2014**, *6*, 314.
[25] A. Dasgupta, X. Yang, J. Gao, *J. Opt.* **2019**, *21*, 125404.
[26] Y. Shan, Y. Li, D. Huang, Q. Tong, W. Yao, W. T. Liu, S. Wu, *Sci. Adv.* **2018**, *4*, eaat0074.
[27] W. T. Hsu, Z. A. Zhao, L. J. Li, C. H. Chen, M. H. Chiu, P. S. Chang, Y. C. Chou, W. H. Chang, *ACS Nano* **2014**, *8*, 2951.
[28] L. Mennel, M. Paur, T. Mueller, *APL Photonics* **2019**, *4*, 034404.
[29] M. J. L. F. Rodrigues, C. J. S. de Matos, Y. W. Ho, H. Peixoto, R. E. P. de Oliveira, H. Y. Wu, A. H. C. Neto, J. Viana-Gomes, *Adv. Mater.* **2016**, *28*, 10693.
[30] N. Youngblood, R. Peng, A. Nemilentsau, T. Low, M. Li, *ACS Photonics* **2017**, *4*, 8.
[31] A. Autere, C. R. Ryder, A. Säynätjoki, L. Karvonen, B. Amirsolaimani, R. A. Norwood, N. Peyghambarian, K. Kieu, H. Lipsanen, M. C. Hersam, Z. J. Sun, *J. Phys. Chem. Lett.* **2017**, *8*, 1343.
[32] Q. Cui, R. A. Muniz, J. E. Sipe, H. Zhao, *Phys. Rev. B* **2017**, *95*, 165406.
[33] S. C. Liu, Y. Mi, D. J. Xue, Y. X. Chen, C. He, X. Liu, J. S. Hu, L. J. Wan, *Adv. Electron. Mater.* **2017**, *3*, 1700141.
[34] D. J. Xue, S. C. Liu, C. M. Dai, S. Chen, C. He, L. Zhao, J. S. Hu, L. J. Wan, *J. Am. Chem. Soc.* **2017**, *139*, 958.
[35] X. Lv, W. Wei, C. Mu, B. Huang, Y. Dai, *J. Mater. Chem. A* **2018**, *6*, 5032.
[36] X. Zhou, X. Hu, B. Jin, J. Yu, K. Liu, H. Li, T. Zhai, *Adv. Sci.* **2018**, *5*, 1800478.
[37] D. J. Xue, J. Tan, J. S. Hu, W. Hu, Y. G. Guo, L. J. Wan, *Adv. Mater.* **2012**, *24*, 4528.
[38] B. Mukherjee, Y. Cai, H. R. Tan, Y. P. Feng, E. S. Tok, C. H. Sow, *ACS Appl. Mater. Interfaces* **2013**, *5*, 9594.
[39] H. C. Hsueh, J. X. Li, C. H. Ho, *Adv. Opt. Mater.* **2018**, *6*, 1701194.
[40] Y. Yang, S. C. Liu, Y. Wang, M. Long, C. M. Dai, S. Chen, B. Zhang, Z. Sun, Z. Sun, C. Hu, S. Zhang, L. Tong, G. Zhang, D. J. Xue, J. S. Hu, *Adv. Opt. Mater.* **2019**, *7*, 1801311.
[41] X. Wang, Y. Li, L. Huang, X. W. Jiang, L. Jiang, H. Dong, Z. Wei, J. Li, W. J. Hu, *J. Am. Chem. Soc.* **2017**, *139*, 14976.
[42] S. Yang, Y. Liu, M. Wu, L. D. Zhao, Z. Lin, H. C. Cheng, Y. Wang, C. Jiang, S. H. Wei, L. Huang, Y. Huang, X. Duan, *Nano Res.* **2018**, *11*, 554.
[43] R. W. Boyd, *Nonlinear Optics*, Academic Press, San Diego, CA **2003**.
[44] X. L. Yang, S. W. Xie, *Appl. Opt.* **1995**, *34*, 6130.
[45] A. Säynätjoki, L. Karvonen, J. Riikonen, W. Kim, S. Mehravar, R. A. Norwood, N. Peyghambarian, H. Lipsanen, K. Kieu, *ACS Nano* **2013**, *7*, 8441.